Computational Fluid Dynamics and Population Balance Model Enhances the Smart Manufacturing and Performance Optimization of an Innovative Precipitation Reactor

processes

MDPI

Article

Computational Fluid Dynamics and Population Balance Model Enhances the Smart Manufacturing and Performance Optimization of an Innovative Precipitation Reactor

Antonello Raponi [1,*,†], Diego Fida [1], Fabrizio Vicari [2], Andrea Cipollina [3] and Daniele Marchisio [1]

[1] Department of Applied Science and Technology, Institute of Chemical Engineering, Politecnico di Torino, 10129 Torino, Italy; diego.fida@polito.it (D.F.); daniele.marchisio@polito.it (D.M.)
[2] ResourSEAs srl, 90141 Palermo, Italy; fabrizio.vicari@resourseas.com
[3] Dipartimento di Ingegneria, Università degli Studi di Palermo—Viale delle Scienze Ed.6, 90128 Palermo, Italy; andrea.cipollina@unipa.it
* Correspondence: antonello.raponi@polito.it
† Current address: Davidson School of Chemical Engineering, Purdue University, West Lafayette, IN 47907, USA.

Abstract: In this study, we propose the study of an innovative precipitation prototype designed by ResourSEAs, guided by a CFD-PBM (Computational Fluid Dynamics and Population Balance Model) approach, aiming to understand the influence of reactant concentration and nozzle orientation on precipitation processes. The first part of the study examines the effect of reactant concentration on supersaturation and the zeroth-order moment (m_0) within a controlled flow and turbulence fields. Three different concentrations of Mg^{2+} (0.1, 0.3, and 0.6 M) and OH^- (0.005, 0.01, and 0.02 M) were tested, resulting in varying supersaturation profiles and m_0 fields. Our results show that, under equal turbulence conditions, increasing the concentration of reactants beyond a certain point actually slows down mixing, which in turn hinders the generation of supersaturation. As a result, supersaturation profiles become nearly identical to those of lower concentrations, despite having consumed more reactants. The second part of this study focuses on the effect of nozzle orientation and positioning along the prototype axis on reactant mixing and particle formation. The simulations reveal that nozzle orientation has a significant impact on the formation of primary particles, especially when positioned in low-velocity regions, leading to slower mixing and greater particle growth. Conversely, high-velocity regions promote faster mixing and more intense aggregation. These findings highlight the interplay between concentration, nozzle orientation, and flow conditions in determining precipitation efficiency, offering insights for optimizing reactor design in industrial applications.

Keywords: population balance modelling; smart manufacturing; digital twins; computational fluid dynamics; magnesium hydroxide precipitation

Academic Editor: Krzysztof Rogowski

Received: 11 April 2025
Revised: 5 May 2025
Accepted: 14 May 2025
Published: 31 May 2025

Citation: Raponi, A.; Fida, D.; Vicari, F.; Cipollina, A.; Marchisio, D. Computational Fluid Dynamics and Population Balance Model Enhances the Smart Manufacturing and Performance Optimization of an Innovative Precipitation Reactor. *Processes* **2025**, *13*, 1721. https://doi.org/10.3390/pr13061721

1. Introduction

In recent years, Mg has been included in the critical raw materials list. As a consequence, the number of studies on how to recover it from non-conventional sources, such as waste brines or bitterns, has increased. In this regard, the synthesis of $Mg(OH)_2$ is one of the most widely used means of recovery, due the multitude of applications in which $Mg(OH)_2$ can be employed [1–7].

The first recovery route was the hydrothermal process [8], which was replaced due to its high energy demand. Therefore, less energetic alternatives have attracted attention [9]. One of them is the precipitation [10] of $Mg(OH)_2$ from brines or bitterns as a

result of the reaction between the Mg^{2+} and an alkaline solution (e.g., NaOH). The reaction produces increasing supersaturation levels that, in turn, directly trigger primary (or molecular) processes, such as primary nucleation and molecular growth. The occurrence of primary processes leads to the formation of 'primary particles'. In addition to the molecular processes, secondary processes can occur, as follows: (i) agglomeration (weak physical interaction between primary particles due to the presence of liquid) and (ii) aggregation (strong chemical interaction resulting in the formation of a crystalline bridge between primary particles) [11].

The presence of processes occurring at the molecular scale (i.e., primary nucleation and growth), at the meso-scale (i.e., agglomeration and aggregation), and at the macro-scale (i.e., fluid motion) make precipitation a complex process whose modelling needs to account for this multi-scale nature. Due to the fast rates, one of the key aspects to account for in precipitation is mixing at all scales [12–14]. In fact, the combination of macro- and micro-mixing determines how fast (or slowly) the reactant reach the molecular scale (i.e., the Batchelor scale) and react influencing all the precipitation phenomena downstream. Although in some cases the mixing modelling in precipitation can be neglected [15], in the majority of cases it is essential to include it. Danckwerts [16], Becker and Larson [17] were among the first to introduce the micro-mixing effect in fast reactions. In recent years, with the increase in computing power, many researchers have studied the influence of mixing on various processes by resorting to Computational Fluid Dynamics (CFD) simulations and experimental validation [18]. Schikarski et al. [19,20] proposed a detailed numerical assessment and experimental validation of the mixing in static mixers, employing Direct Numerical Simulations (DNS). On the other hand, less computationally expensive approaches can be used. Shiea et al. [21] proposed a Reynolds-Averaged Navier–Stokes equation (RANS) approach and a multi-environment model to integrate the micro-mixing effect in the co-precipitation modelling of Ni-Mn-Co hydroxide. Analogously, in previous publications of ours, we introduced a Population Balance Model (PBM) coupled with CFD simulations in the RANS framework to model $Mg(OH)_2$ precipitation. We built the model [22], tuned it by identifying its parameters [23] using a novel machine learning methodology, and validated it [24].

In this contribution, we use the same validated model to assess the effect of variation in design parameters within the possible range covered by the producer of the prototype by investigating the influence of turbulence and, consequently, mixing on the precipitation process. In Section 2, the prototype is presented and Large Eddy Simulations (LES) are exploited to characterize and validate the flow field due to the lack of experimental data corresponding to the study. In Section 3, we introduce the CFD-PBM model, emphasizing the relationship between turbulence, mixing, and precipitation phenomena. To conclude, in Section 4, we present two cases. The first assesses the influence of the reactant concentration at constant flow rates on precipitation, while the second assesses the influence of turbulence and, therefore, mixing on the precipitation process as a function of the feeding zone. Lastly, in Section 6, we draw relevant conclusions.

2. Materials and Methods

In recent years, a collaborative effort between ResourSEAs srl and the University of Palermo led to the development and construction of a pilot-scale prototype for $Mg(OH)_2$ precipitation to recover Mg^{2+} from various kinds of brines [25]. This system has since been patented by ResourSEAs srl [26]. However, at first, the design process was led by trial and error rather than following any guidelines suggested by a numerical framework. This work aims to bridge this gap, demonstrating the practical value of modelling approaches in the context of smart manufacturing. In this work, we go through an analysis of the design

parameters, exploring the ranges covered by the patent, to optimize the performance of the prototype. The prototype features a tubular design with several inlet streams and can be mathematically described as a Multi-Feed Plug Flow Reactor (MF-PFR). A schematic illustration of the MF-PFR is shown in Figure 1.

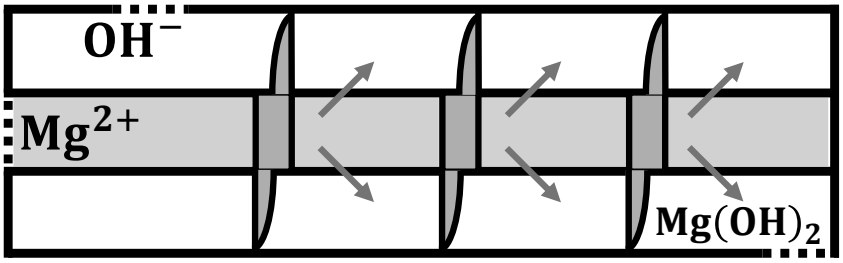

Figure 1. MF-PFR schematic representation.

The prototype consists of an inner and outer tube, and the two environments exchange transport properties thanks to the presence of nozzles. Along the reactor, there are propellers whose purpose is to create a rotational motion to promote the mixing of reactants. $MgCl_2$ is fed into the inner tube, and NaOH into the outer crown. The reactants, therefore, react in the outer crown according to the following reaction:

$$Mg^{2+}{}_{(aq)} + 2OH^{-}{}_{(aq)} \rightarrow Mg(OH)_{2(s)} \downarrow \quad (1)$$

To preserve confidentiality, all parameters subject to patent protection are expressed in a dimensionless form. However, the analysis that guided the design and performance optimization is provided in full. Given the periodic nature of the device, where identical mixing conditions repeat between consecutive propellers, our study focuses on the precipitation process that occurs between two propellers. This approach allows us to isolate and investigate the impact of local mixing conditions on the precipitation process while maintaining the representativeness of the overall behavior of the prototype. For the sake of clarity, the wireframe of the geometry is presented in Figure 2.

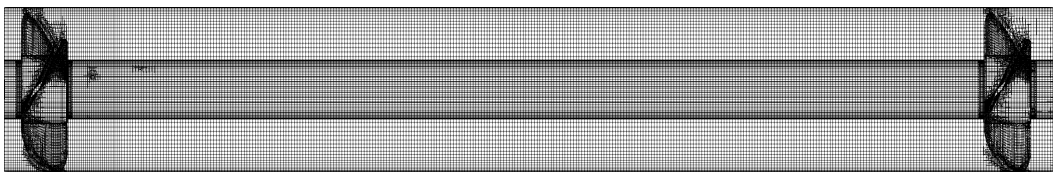

Figure 2. Geometry wireframe.

The geometry presented in Figure 2 is our template. This means that, depending on the operating conditions, we changed the length of the tubes, the number of nozzles, and their position and/or orientation, but we kept the propeller type, its orientation, and the tube diameters constant. Further details on the mesh and grid convergence are reported in the 'Supplementary Materials'.

Flow Field and Turbulence Model and Simulation Setup

The formation of low-solubility compounds is strongly influenced by mixing behavior, and thus by the fluid flow characteristics of the system. At high *Re* numbers, the choice of turbulence model can substantially impact the predicted flow patterns and, consequently, the precipitation outcomes [15,24]. In the absence of experimental data, Large Eddies Simulations (LES) offer higher accuracy compared to Reynolds-Averaged Navier–Stoke (RANS) models, but are much more time-consuming. Therefore, the LES were used to select the RANS model that was best able to mimic the LES steady-state solution. In LES, the

large-scale turbulent structures (eddies), which carry most of the turbulent kinetic energy, are solved explicitly, whereas the smaller subgrid-scale (SGS) eddies are modeled. The LES methodology is based on the filtered Navier–Stokes equations, which separate the velocity field, u, into a resolved component, $\bar{u}$, and a subgrid-scale component, u'. Therefore, by substituting the decomposed velocity and employing the Boussinesq hypothesis, the Navier–Stokes equations, for an incompressible Newtonian fluid, become the following:

$$\frac{\partial \mathbf{u}^{(GS)}}{\partial t} + \mathbf{u}^{(GS)} \cdot \nabla \mathbf{u}^{(GS)} = -\frac{1}{\rho}\nabla p^{(GS)} + (\nu + \nu_t)\nabla^2 \mathbf{u}^{(GS)} + \mathbf{g} \quad (2)$$

where $\bar{p}$ is the pressure field, ρ is the fluid density, ν is the kinematic viscosity and $\mathbf{g}$ is the gravitational acceleration. ν_t is the turbulent kinematic viscosity and it is approximated using a turbulence model. The RANS approach, on the other hand, relies on time-averaging the Navier–Stokes equations, decomposing the velocity field into mean and fluctuating components. Unlike LES, where only the smallest scales are modelled, RANS models approximate the entire turbulence spectrum, making them computationally cheaper but potentially less accurate. In this contribution, the RANS model candidates include the standard $k-\varepsilon$, $k-\varepsilon$ RNG, and $k-\omega$ SST. The LES candidate, instead, is the k-equation (kEq) model, a one-equation LES model. In Table 1, we report the boundary conditions (BC).

Table 1. Boundary conditions used for the simulations.

Boundary	Velocity	Pressure	Turbulence Fields
Inlet	Flowrate	Neumann	Correlation
Outlet	Neumann	0	Neumann
Inner tube	No-slip	Neumann	Wall function
Outer tube	No-slip	Neumann	Wall function
Propeller (stationary)	No-slip	Neumann	Wall function
Nozzles	Flowrate	Neumann	Correlation

To enhance the stability and accelerate the convergence of the LES simulations, these were initialized using the solution derived from the standard $k-\varepsilon$ turbulence model. Each LES run continued for a duration corresponding to 10 residence times, which was sufficient to obtain results statistically independent of the initial conditions [27]. To confirm this independence, an additional LES was initialized using the $k-\omega$ SST model, yielding equivalent results. This validated the assumption that 10 residence times are adequate to eliminate sensitivity to initial conditions. The computational mesh was designed to capture at least 80% of the turbulent kinetic energy [28]. Accordingly, the characteristic grid size was determined by calculating the maximum allowable cell dimension using Equation (3):

$$\max(\Delta) = \frac{1}{5}\min(l_0) \quad (3)$$

l_0 was obtained from the RANS simulation and corresponds to the integral length scale, defined as follows:

$$l_0 = \left(\frac{k^{3/2}}{\varepsilon}\right)^{1/4} = \frac{k^{\frac{1}{2}}}{\omega\, C_\mu^{\frac{1}{4}}} \quad (4)$$

Equation (3), therefore, establishes that the maximum value for the SGS in the LES should not exceed 20% (i.e., 1/5) of the minimum among the largest eddy size (l_0) in the system.

Figure 3 highlights the significant influence of the vortex formed downstream of the blade. This structure corresponds to a fluid region characterized by high residence times. A comparison of the vortex dimensions clearly reveals that the standard $k-\varepsilon$

model (Figure 3a) yields results that markedly deviate from those obtained with the other turbulence models. In the case of the standard $k-\varepsilon$ model, the vortex does not extend far beyond the propeller, whereas all the others develop a vortex with a dimensionless axial coordinate of 0.2. A quantitative assessment was also performed by calculating, for each cell, the error in the turbulent kinetic energy. For RANS, the turbulent kinetic energy field (k_{RANS}) was directly available through obtaining the solution of the transport equation for k. For LES, the turbulent kinetic energy field (k_{LES}) was reconstructed as the sum of the modelled contribution, $k^{(SGS)}$, and the resolved contribution, $k^{(GS)}$. The former was immediately available from the LES simulation, whereas the latter was calculated as follows:

$$k^{(GS)} = \frac{1}{2}\sum_i u_i' u_i' \tag{5}$$

where u' is the fluctuating velocity. This was calculated as the difference between the resolved velocity and its time average. The error for the i-th cell, therefore, was defined as follows:

$$\varphi_{\mathrm{err},i} = \frac{|k_{\mathrm{RANS},i} - k_{\mathrm{LES},i}|}{\max(k_{\mathrm{RANS},i}, k_{\mathrm{LES},i})} \tag{6}$$

Through construction, this will tend toward 0 if the RANS and LES values overlap in the i-th cell and toward 1 if their values deviate. The distribution function of the error was defined as follows:

$$f_i(\varphi) = \frac{\sum_j V_j}{V_{tot}} \frac{1}{\varphi_{\mathrm{err},i+1} - \varphi_{\mathrm{err},i}} \tag{7}$$

$$\sum_i [f_i(\varphi)(\varphi_{i+1} - \varphi_i)] = 1 \tag{8}$$

Equation (7) represents the volume fraction of the system, whose error is between $\varphi_{\mathrm{err},i}$ and $\varphi_{\mathrm{err},i+1}$.

Figure 4 presents a comparison of the error distribution functions for the three RANS models and the k-Eq model. The results indicate a notable deviation for the k when using the standard $k-\varepsilon$ model. The distribution function shows higher values in bins closer to 1, leading to an average error that is nearly four orders of magnitude larger than those obtained with the k-Eq model. Both the $k-\varepsilon$ RNG and $k-\omega$ SST models exhibit large regions where the turbulent kinetic energy values are in close agreement with those obtained from the LES simulations. Furthermore, while the difference is relatively small, it is worth noting that the $k-\varepsilon$ RNG and $k-\omega$ SST models also show some discrepancies compared to LES, particularly in the reactor region before the propellers, an area that is not directly impacted by the reactants. This discrepancy can be attributed to the absence of vortex formation before the blades, resulting in a solution with a lower-intensity turbulence and fewer explicitly resolved features. As a consequence, the standard $k-\varepsilon$ model produces results that significantly differ from those of the other models, which are more consistent with one another. A comparison was performed between the $k-\varepsilon$ RNG and $k-\omega$ SST models using an analogous error metric defined as follows:

$$\varphi_{\mathrm{err}_2,i} = \frac{|k_{k-\varepsilon\ \mathrm{RNG},i} - k_{k-\omega\ \mathrm{SST},i}|}{max(k_{k-\varepsilon\ \mathrm{RNG}}, k_{k-\omega\ \mathrm{SST}})} \tag{9}$$

Here, $k_{k-\varepsilon\ RNG}$ and $k_{k-\omega\ SST}$ represent the turbulent kinetic energy values returned from the $k-\varepsilon$ RNG and $k-\omega$ SST models, respectively. The distribution function is shown in Figure 5.

The turbulence models predict comparable results, with an average error of 0.3. In conclusion, the standard $k-\varepsilon$ model was excluded for the reasons discussed earlier, and

the $k-\omega$ SST model was selected. Similar to the $k-\omega$ SST model, the $k-\varepsilon$ RNG also produces results in line with the LES simulations. However, the $k-\omega$ SST model was preferred over the $k-\varepsilon$ RNG due to its lower computational cost.

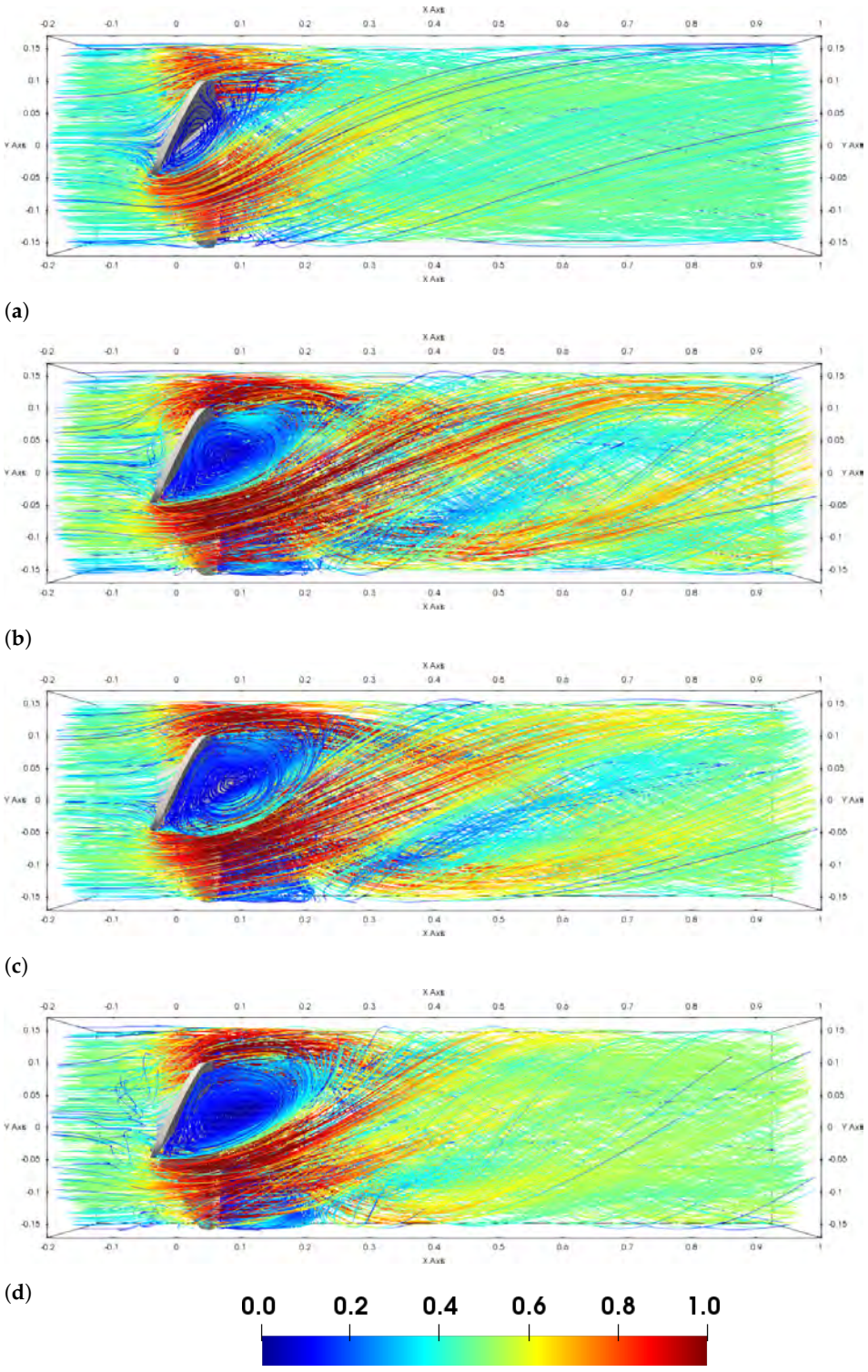

Figure 3. Velocity field displayed on streamlines for (**a**) standard $k-\varepsilon$; (**b**) $k-\varepsilon$ RNG; (**c**) $k-\omega$ SST; and (**d**) k-Eq.

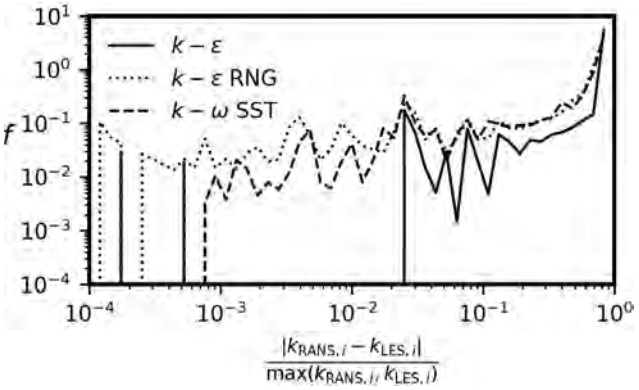

Figure 4. Error distribution function comparing LES with RANS simulations. Standard $k-\varepsilon$ (solid line); $k-\varepsilon$ RNG (dotted line); and $k-\omega$ SST (dashed line).

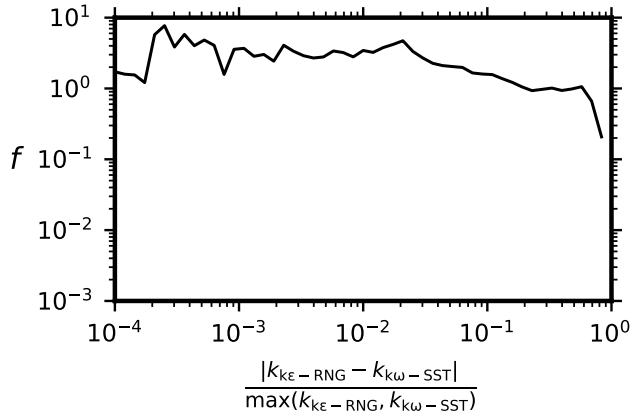

Figure 5. Error distribution function comparing the $k-\varepsilon$ RNG and $k-\omega$ SST models.

3. Population Balance Model

In this section, the employed PBM is detailed. As mentioned in Section 2, the interplay between fluid dynamics and precipitation determines the final primary particles. In this contribution, the coupling between the fluid dynamics and the precipitation phenomena was obtained through implementing the β-Probability Density Function (PDF) approach. In this approach, two equations are used to model the multi-scale nature of precipitation. One equation is employed to track the evolution of the mixture fraction, $\bar{\alpha}$, and the other is used to track the evolution of the variance in the mixture fraction, $\bar{\alpha}'^2$. The mixture fraction describes the macro-mixing, whereas its variance describes the micro-mixing. In the RANS framework, the transport equation for $\bar{\alpha}$ is as follows:

$$\frac{\partial \bar{\alpha}}{\partial t} + \bar{\mathbf{u}}\nabla\bar{\alpha} = D_t\nabla^2\bar{\alpha} \tag{10}$$

and the transport equation for its variance is as follows:

$$\frac{\partial \bar{\alpha}'^2}{\partial t} + \bar{\mathbf{u}}\cdot\nabla\bar{\alpha}'^2 = D_t\nabla^2\bar{\alpha}'^2 + 2D_t(\nabla\bar{\alpha}\cdot\nabla\bar{\alpha}) - \epsilon_{\bar{\alpha}'^2} \tag{11}$$

In addition to the accumulation, advection, and diffusion, Equation (11) has two other terms to analyze. The production term, $2D_t(\nabla\bar{\alpha}\cdot\nabla\bar{\alpha})$, is related to the macro-scale, where variance is generated, and the dissipation term $\epsilon_{\bar{\alpha}'^2}$, is related to the smallest scale (i.e., the

Batchelor scale), where it is dissipated. Unlike the production, the dissipation term requires a closure equation [13]:

$$\epsilon_{\bar{\alpha}'^2} = \gamma\overline{\alpha'^2} \tag{12}$$

$$\gamma = \frac{C_\phi}{2}\frac{\varepsilon}{k} \tag{13}$$

According to our previous publications [22,24], C_ϕ was set to be equal to 2. This approach, therefore, can account for the dumping effect of mixing on the chemical reaction. In other words, Mg^{2+} and OH^- have to macro- and micro-mix before they can react according to Equation (1), hindering the precipitation process. In our previous publication [22] (Supplementary Materials), we derived an analytical solution through coupling the reactant concentration htat was fed into the system with the amount that is physically able to react (i.e., the amount of reactants at the micro-scale) after mixing to form the $Mg(OH)_2$. For the sake of clarity, only the final equation is reported:

$$[Mg(OH)_2]_{(aq)} = \min\left(\left[Mg^{2+}\right], \frac{[OH^-]}{2}\right) f\left(\bar{\alpha}, \bar{\alpha}'^2, \bar{\alpha_s}\right) \tag{14}$$

where Mg^{2+} and OH^- are the concentration values in the system and $f\left(\bar{\alpha}, \bar{\alpha}'^2, \bar{\alpha_s}\right)$ is the weighting function accounting for mixing. $\bar{\alpha}_s$ is the stoichiometric mixture fraction, defined as follows:

$$\bar{\alpha}_s = \frac{2\left[Mg^{2+}\right]^{(in)}}{2[Mg^{2+}]^{(in)} + [OH^-]^{(in)}} \tag{15}$$

where apex "(in)" represents the reactant concentration at the inlets. This represents, in the mixture fraction space, the mixture fraction value at which the reactants can stoichiometrically react. Assuming that the $Mg(OH)_{2(aq)}$ in the aqueous phase instantaneously precipitates in its solid form, we can define the supersaturation as follows:

$$S = \frac{\gamma_\pm^3 [Mg^{2+}]_{(aq)} [OH^-]^2_{(aq)}}{k_{sp}} - 1 \tag{16}$$

where $[Mg^{2+}]_{(aq)}$ and $[OH^-]_{(aq)}$ are calculated for stoichiometry using Equation (14), $\gamma_\pm$ is the activity coefficient, and k_{sp} is the solubility product, which is equal to $10^{-10.88}$. Supersaturation build-up, therefore, triggers precipitation processes. In this contribution, we accounted for primary nucleation (both homogeneous and heterogeneous), J:

$$J = \underbrace{A_1 e^{\left(-\frac{B_1}{\ln^2(S+1)}\right)}}_{\text{Homogeneous}} + \underbrace{A_2 e^{\left(-\frac{B_2}{\ln^2(S+1)}\right)}}_{\text{Heterogeneous}} \tag{17}$$

and molecular growth, G:

$$G = k_g S^g \tag{18}$$

Equations (17) and (18) have six tuning parameters (A_1, B_1, A_2, B_2, k_g, and g). A_i and B_i model the intensity of primary nucleation, k_g represents the intensity of the molecular growth, and g is related to the growth mechanism (g = 1 corresponds to a diffusion-controlled mechanism). The aggregation rate, β_{agg}, is as follows:

$$\beta_{agg} = \beta_{col}\eta_{agg} \tag{19}$$

The aggregation rate is proportional to the collision frequency, β_{col}, representing the number of collisions per unit time between primary particles, and to the sticking probability, η_{agg},

which represents the probability that these events are effective (i.e., whether the primary particle will cement or not). The collision frequency accounts for both the Brownian and turbulent contributions.

$$\beta_{\mathrm{col}} = 10^{C_1}(\beta_{\mathrm{br}} + \beta_{\mathrm{tr}}) \tag{20}$$

The Brownian contribution is described by the following equation:

$$\beta_{\mathrm{br}} = \frac{2k_{\mathrm{B}}T}{3\mu}\frac{(L+\lambda)^2}{L\lambda} \tag{21}$$

where k_{B} is the Boltzmann constant, T is the fluid temperature, μ is the fluid dynamic viscosity, and L and λ are the sizes of the colliding particles. The turbulent contribution, instead, has the following form:

$$\beta_{\mathrm{tr}} = \sqrt{\frac{8\pi}{15}}\sqrt{\frac{\varepsilon}{\nu}}\frac{(L+\lambda)^3}{2} \tag{22}$$

The sticking probability equation, on the other hand, can be modelled as follows:

$$\eta_{\mathrm{agg}} = e^{-\theta} \tag{23}$$

where θ denotes the ratio of the cementation time, t_{cem}, and the interaction time, t_{int}. The interaction time is defined as the characteristic time of the Kolmogorov micro-scale:

$$t_{\mathrm{int}} = \sqrt{\frac{\nu}{\varepsilon}} \tag{24}$$

and represents the duration during which the two particles remain in close proximity and interact, while the cementation time is defined as follows:

$$t_{\mathrm{cem}} = \frac{D_{\mathrm{b}}}{s(\delta)G} \tag{25}$$

$$D_{\mathrm{b}} = \frac{L_{\mathrm{eqv}}\rho_{\mathrm{p}}^{0.5}(\varepsilon\nu)^{0.25}}{A_{\mathrm{p}}^{0.5}} \tag{26}$$

$$L_{\mathrm{eqv}} = \frac{L\lambda}{(L^2+\lambda^2-L\lambda)^{0.5}} \tag{27}$$

This represents the time needed for the irreversible cementation of two primary particles. $s(\delta)$ is a shape function, defined as follows [29]:

$$s(\delta) = \frac{4\left(1+\delta-\delta'\right)}{1/3+\delta-\delta'-\left(\delta-\delta'\right)^2\left(2\delta/3+\delta'/3\right)} \tag{28}$$

$$\delta = L/\lambda \tag{29}$$

$$\delta' = \sqrt{\delta^2-1} \tag{30}$$

Equations (20) and (26) have two additional tuning parameters (C_1 and A_{p}). C_1 modules the collision frequency intensity and A_{p} is proportional to the crystalline bridge strength between primary particles. In our previous publications, we provided innovative machine learning-based methodologies to identify their values [23], fitted our model [22], and validated it [24]. Therefore, only their values are reported here (Table 2).

Table 2. Kinetics parameters set from Raponi and Marchisio [23].

	A_1	A_2	B_1	B_2	k_g	g	C_1	A_p
Parameter value	$10^{25.45}$	$10^{15.4}$	301	57	$10^{-11.15}$	1.5	0.79	5.3
Units	particle no. / $m^3 s^1$		-	-	m / s	-	-	N / m^2

The evolution of the primary particles due to the precipitation phenomena described above was tracked through applying the Quadrature Method of Moments (QMOM) [14,30]. The transport equation for the k-th moment is as follows:

$$\frac{\partial \bar{m}_k}{\partial t} + \bar{\mathbf{u}} \cdot \nabla \bar{m}_k = D_t \nabla^2 \bar{m}_k + \dot{h}_k \quad (31)$$

$$\dot{h}_k = J L_c^k + k G m_{k-1} + \overline{B}_k - \overline{D}_k \quad (32)$$

where L_c is the critical size (1 nm) for a stable nucleus and $\overline{B}_k$ and $\overline{D}_k$ model the birth and death contributions due to aggregation. In this contribution, we used three quadrature nodes, leading to six moments. To conclude, the PBM was closed using the mass balances for the reacting species ($[Mg^{2+}]$ and $[OH^-]$):

$$\frac{\partial \bar{c}_i}{\partial t} + \bar{\mathbf{u}} \cdot \nabla \bar{c}_i = D_t \nabla^2 \bar{c}_i - \frac{\nu_i \rho_p k_v}{M_p} \dot{h}_3 \quad (33)$$

where ν_i is the stoichiometric coefficient (i.e., $\nu_{Mg^{2+}} = 1$ and $\nu_{OH^-} = 2$), ρ_p corresponds to the particle density, M_p is the molecular weight, $k_v = \pi/6$ is the shape factor, and $\dot{h}_3$ is the third-order moment sink term. We used a one-way approach for the CFD-PBM. The flow and turbulence fields extracted from the steady-state RANS solution and passed to the PBM were used as constant inputs. These quantities were used to compute the mixing and aggregation for use in the population balance model. Given the low solids concentration and the sub-micron/micron size of the $Mg(OH)_2$ particles, the particle–fluid interactions are negligible, justifying the one-way coupling approach [22].

4. Results

We report two investigations: (i) the influence of the reactant concentration at constant flow and turbulence fields and (ii) the influence of the nozzles orientation at constant reactant concentrations.

(i) Effect of the reactant concentration

To assess the influence of the reactant concentration, three values for Mg^{2+} concentration (0.1, 0.3, and 0.6 M) and three for OH^- (0.005, 0.01, and 0.02 M) were selected, resulting in a matrix of nine elements. These concentration values were selected to reflect the operational ranges in the pilot plant, based on the inlet flow rates and chemical compositions that are typically handled. The analysis was performed with the same flow and turbulence fields. In this regard, the same geometry only had two nozzles: one pointing in a high-velocity region and another pointing in a low-velocity region. This decision was made so as not to lose generality. Since the geometry is constant, this implies that the mixture fraction and its variance remain constant across all operating conditions. Equations (10) and (11) are functions of the turbulence fields only. Figure 6 shows both the mixture fraction and its variance in the streamlines that the particles would follow if they started from the two nozzles (the model assumes a one-way coupling approach).

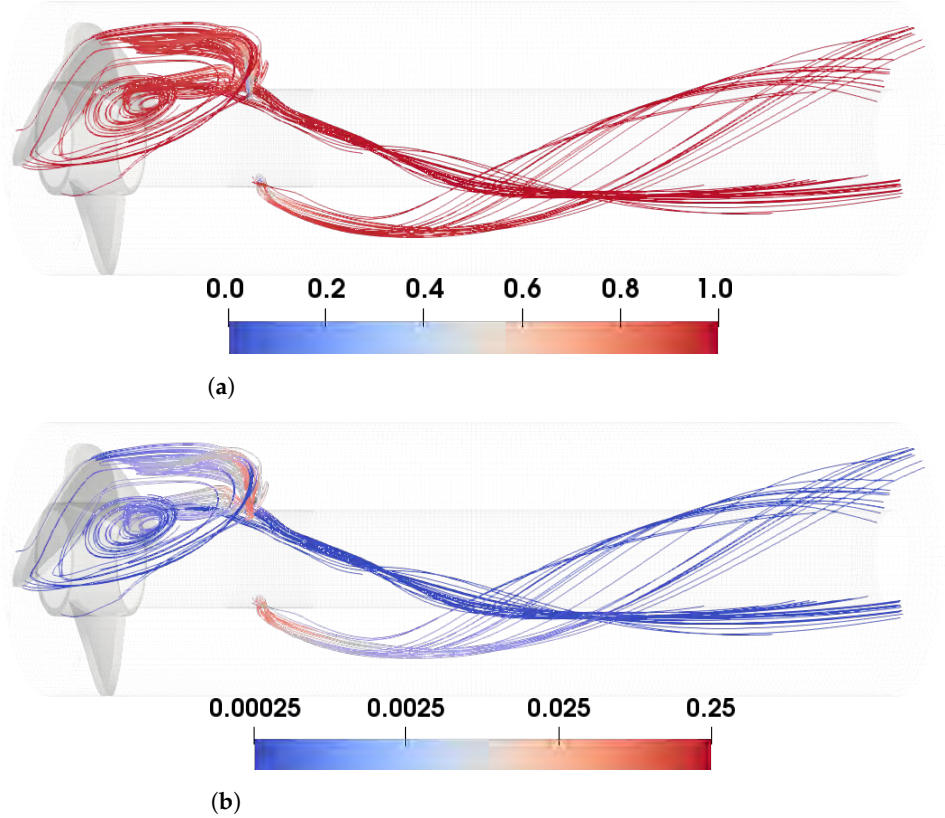

Figure 6. Visualization of the mixture fraction (**a**) and its variance (**b**) for the two nozzles' configuration.

Figure 6 shows that complete mixing occurs soon after the two nozzles. The Mg^{2+} jet entering the circular crown locally alters the mixing fraction (depicted in light blue in Figure 6a). As a result, macro-scale mixing leads to micro-scale segregation, as shown by the red regions around the nozzles in Figure 6b. This investigation, therefore, aims to show how strongly mixing can hinder precipitation processes as a function of the reactant concentration, especially when the ultimate goal is the reactor manufacturing. It is important to emphasize that, even though the flow field, mixture fraction, and its variance remain unchanged across all operating conditions, this does not imply that the mixing conditions are identical. In fact, the mixing weight function in Equation (14) is a function of the stoichiometric mixture fraction, which is a function of the reactant concentration entering the system. As a result, increasing the concentration consistently raises the first term in Equation (14) ($\min([Mg^{2+}], 2[OH^-])$). However, the effect on the second term (f) is not straightforward, as it depends on the local value of $\bar{\alpha}$ relative to $\bar{\alpha_s}$. The corresponding $\bar{\alpha_s}$ values for all nine simulations are listed in Table 3.

Table 3. $\bar{\alpha}_s$ values used in the simulations.

$[Mg^{2+}]^{(in)}$, M	$[OH^-]^{(in)}$, M		
	0.005	**0.01**	**0.02**
0.1	0.976	0.952	0.909
0.3	0.992	0.984	0.968
0.6	0.996	0.992	0.984

The two variables used for comparison are both the supersaturation, S, and the zeroth order moment, m_0. Figure 7 presents the results for the supersaturation.

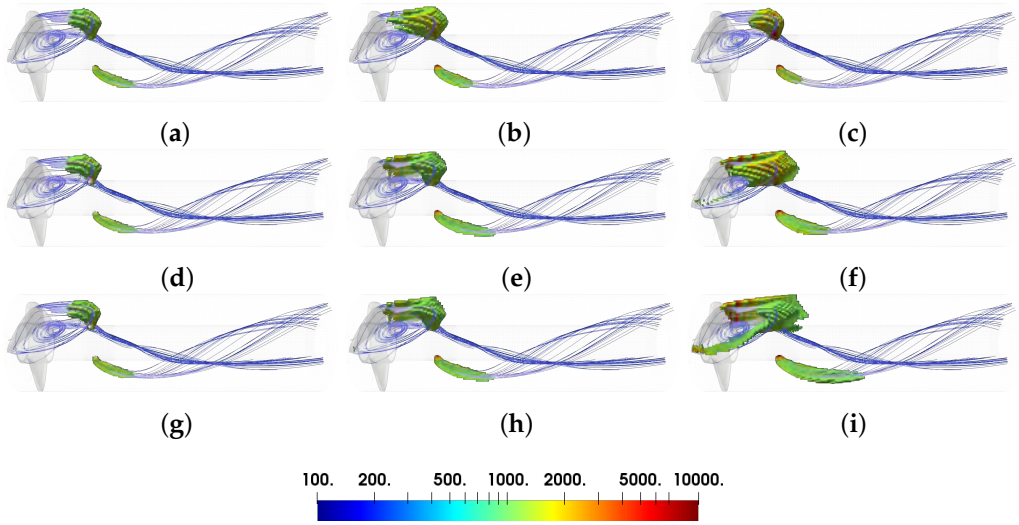

Figure 7. Supersaturation fields. The volumes represented correspond to cells whose supersaturation values are greater than 1000.

Figure 7 illustrates the supersaturation levels obtained within the system. The visualized volumes correspond to computational cells where supersaturation exceeds 1000. The colorbar scale was adjusted to enhance clarity. According to Equation (14), local supersaturation is primarily influenced by the OH^- concentration. When $\bar{\alpha}_s$ shows minimal variation with increasing Mg^{2+} concentration (Table 3, first column), the resulting supersaturation profile remains largely unaffected under constant OH^- levels (cases shown in Figure 7a,d,g). A similar trend is observed when the second column of Table 3 is examined (cases shown in Figure 7b,e,h). On the other hand, by evaluating the trend in the rows in Table 3, more pronounced changes are revealed. For example, $\bar{\alpha}_s$ decreases along the rows, indicating a worsening in mixing efficiency. Meanwhile, the OH^- concentration increases, enhancing supersaturation. These opposing effects compete with each other. As an example, in the cases shown in Figure 7a,b, the increase (doubling) in OH^- concentration dominates, leading to both higher supersaturation levels and a larger affected volume. However, when OH^- is further increased (doubled again), as shown in Figure 7b,c, the sharper decrease in $\bar{\alpha}_s$ results in a reduced supersaturation volume, demonstrating that a worsened mixing can limit precipitation despite higher reactant levels. To ensure meaningful comparisons, the simulation matrix includes case pairs with identical mixing conditions. Specifically, cases Figure 7d,h, as well as cases Figure 7e,i, share the same $\bar{\alpha}_s$ values (0.992 and 0.984, respectively). In these instances, the f term in Equation (14) remains constant, isolating the effect of increasing reactant concentrations. As expected, higher concentrations lead to an increased supersaturation and precipitation volume. Thus, unless extremely high supersaturation and extended precipitation zones are desired (as in Figure 7f,i), using lower OH^- concentrations can be advantageous. This strategy allows for comparable supersaturation profiles with reduced reagent consumption and, consequently, lower operational costs. The analysis is reinforced through the results obtained for m_0, shown in Figure 8.

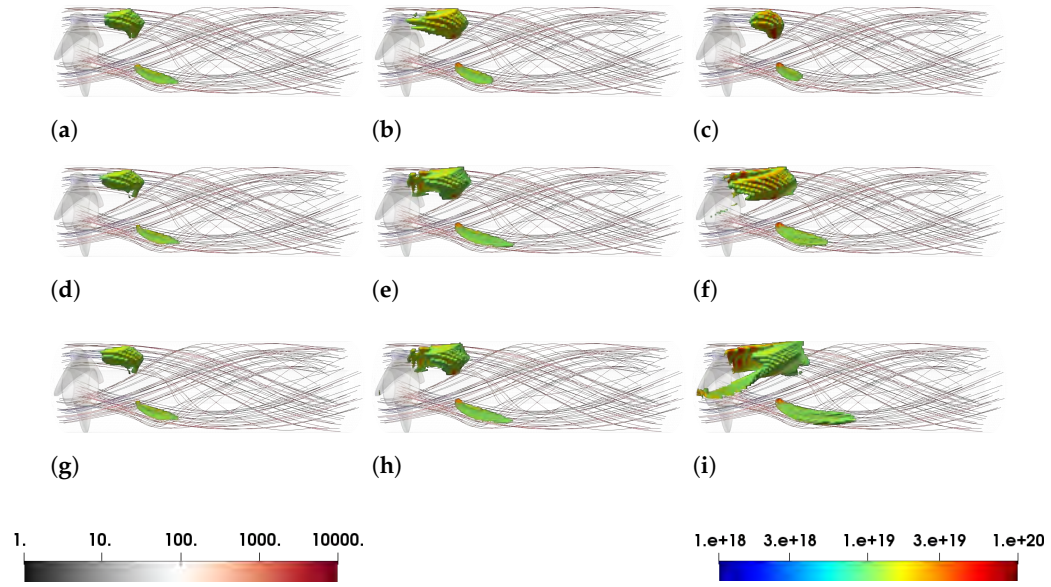

Figure 8. Representation of the ε field on the flow streamlines and m_0 fields. The volumes represented correspond to cells whose m_0 values are greater than 10^{19}.

In Figure 8, the streamlines represent the path a particle takes in the fluid, and the field reported on the streamlines is the epsilon field. It is important to note that, under constant flow and turbulence fields, the spatial distribution of supersaturation solely drives and modulates particle formation. Indeed, the zeroth moment, m_0, depends exclusively on nucleation and aggregation phenomena which, at a constant-turbulence field (ε), are governed by the local supersaturation levels. As reported in Equation (17), nucleation is a direct function of supersaturation, while aggregation is indirectly influenced through the sticking probability (Equations (19), (23) and (25)). The sticking probability depends on the crystal growth rate G, which, in turn, is a function of the local supersaturation. Therefore, the variations observed in the m_0 profiles across the different cases reflect the impact of the supersaturation field on precipitation performance when hydrodynamic conditions are fixed. For example, comparing Figure 8a,b, the increase in OH^- concentration (doubling) leads to a clear increase in m_0, both in terms of absolute values and spatial extent. This occurs despite a slight reduction in the stoichiometric mixture fraction, $\bar{\alpha}_s$. However, when the OH^- concentration is further doubled (shown in Figure 8b,c), $\bar{\alpha}_s$ decreases more significantly and a noticeable reduction in the extent of the m_0 field is observed. Therefore, the analysis of the supersaturation profiles directly informs the interpretation of the m_0 field, as similar trends and effects can be observed.

(ii) Effect of the nozzle's orientation and position

We present and discuss the results of the nozzle's orientation and position in the prototype at constant reactant concentrations and flow rates. In other words, this investigation shows the influence of turbulence on particle formation. A total of six simulations (2×3 cases) were conducted, combining different nozzle orientations (two cases) and different positions along the prototype axis (three cases). For the nozzle orientation, the mutual angular position was not changed. The nozzles were positioned at equal angular intervals of 120° around the circumference of the inner tube. The two cases shown for the orientation refer to the injection of Mg^{2+} into the zone of the circular crown with a low (L) fluid velocity and high (H) fluid velocity. It is noteworthy that the nozzle orientation was adapted to the helicoid flow field developed within the system so that the Mg^{2+} was always fed into the low-fluid-velocity or the high-fluid-velocity zone. These two cases were repeated at three axial coordinates, resulting in six simulations. For the

sake of confidentiality, the axial positions were made dimensionless and were at 0.1, 0.2, and 0.6 of the dimensionless length $\tilde{L}$. Figure 9 shows the six simulation setups reporting the velocity field when the nozzles' orientation ((L) or (H)) and position ($\tilde{L}$ = 0.1 or 0.2 or 0.6) were varied:

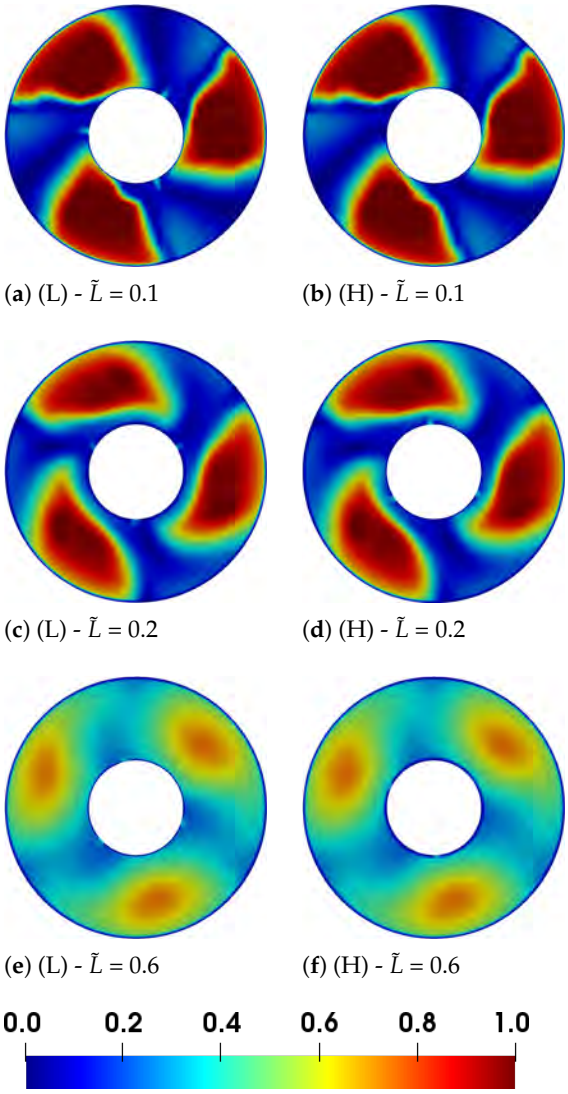

Figure 9. Nozzle configuration: velocity magnitude fields for the feed sections across the six simulated scenarios.

As is clear from Figure 9, the nozzle orientation does not affect the flow field since the Mg^{2+} flow-rate is much smaller compared to the OH^{-} one. For this reason, the ϵ field is reported for only one orientation case (H) at the three different positions along the prototype axis, as shown in Figure 10.

To ensure the same reaction volume (i.e., the same reaction length), simulations were run on a geometry comprising the investigated block plus a portion of the following block, which was equal to the investigated nozzle positions, at 0.1, 0.2, and 0.6 respectively, as reported in Figure 11.

Figures 9 and 11 show interesting results. The orientation of the nozzles has a massive impact (Figure 11a,b) when the nozzles are located at a dimensionless coordinate of 0.1. Figures 9a,b and 10a show that the flow and turbulence fields in the Mg^{2+} feed are very different for the two cases. For the (L) case (Figure 11a), Mg^{2+} reacts in a region where velocity and local turbulence are smaller. It follows that mixing is slower and aggregation

is less favored, as it is directly proportional to $\sqrt{\varepsilon}$. This is the reason why a larger prototype volume has higher m_0 values. Particles nucleate and grow more than they aggregate. On the other hand, for the (H) case (Figure 11b) the Mg^{2+} reacts in a region where velocity and local turbulence are much more intense. It follows that mixing is much faster and aggregation much more intense as it is demonstrated by the evolution m_0. At a dimensionless coordinate of 0.2, the effect becomes less intense, as shown in Figure 11c,d. Figure 9c,d show that the vortex is no longer adjacent to the inner tube and, consequently, the local turbulence found in both cases is similar (Figure 10b). The main change in the m_0 profiles depends on the vortex that the three Mg^{2+} jets encounter. Finally, the effect of the nozzle orientation at a dimensionless coordinate of 0.6 (Figure 11e,f) is practically negligible. This is due to the flow (Figure 9e,f) and turbulence (Figure 10c) fields, which become dampened (and homogenized) by the pressure drops. Therefore, regardless of the orientation, the three nozzles see similar turbulence levels, and the trend of m_0 is nearly the same. To conclude, depending on the manufacturing goal, a decision can be made [31]. If larger particles are preferred, a condition closer to the one in Figure 11a should be preferred. On the other hand, if aggregates are required, a condition in which mixing is faster and turbulence is more intense, namely, a condition closer to the one in Figure 11b, should be preferred.

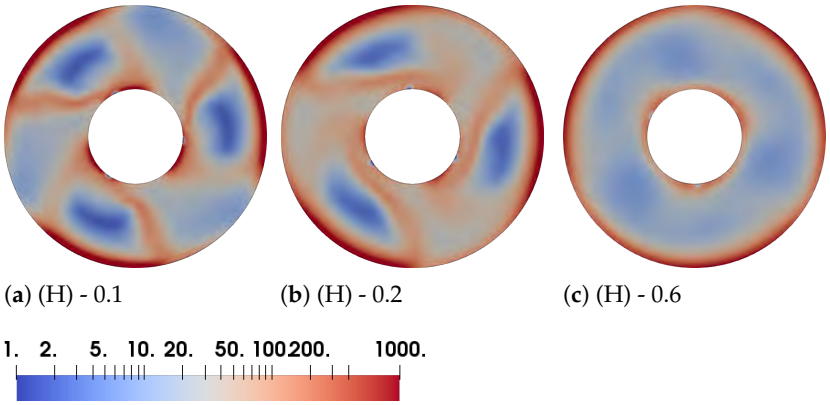

(**a**) (H) - 0.1 (**b**) (H) - 0.2 (**c**) (H) - 0.6

Figure 10. ε field for the (H) orientation at the three different positions along the prototype axis: 0.1 (**a**), 0.2 (**b**), and 0.6 (**c**).

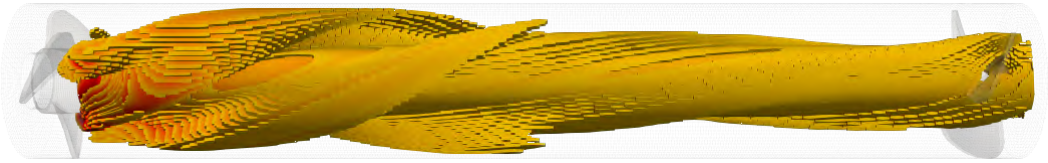

(**a**) (L) - 0.1

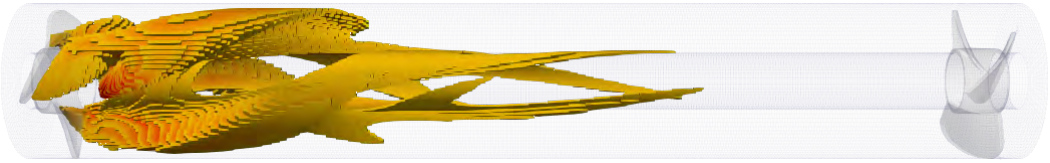

(**b**) (H) - 0.1

Figure 11. *Cont.*

(**c**) (L) - 0.2

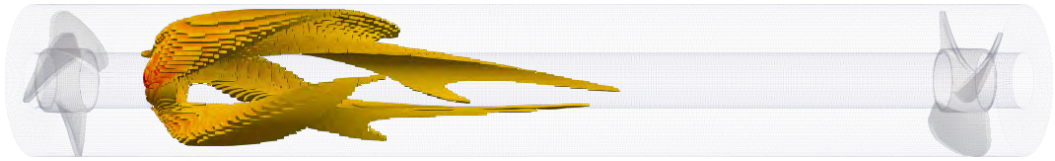

(**d**) (H) - 0.2

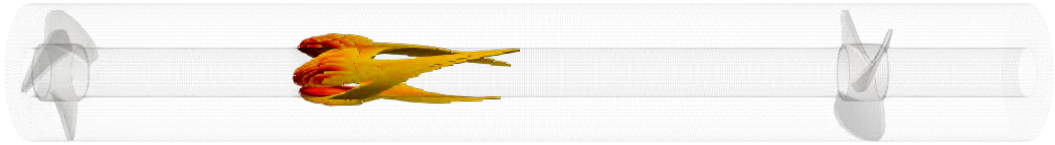

(**e**) (L) - 0.6

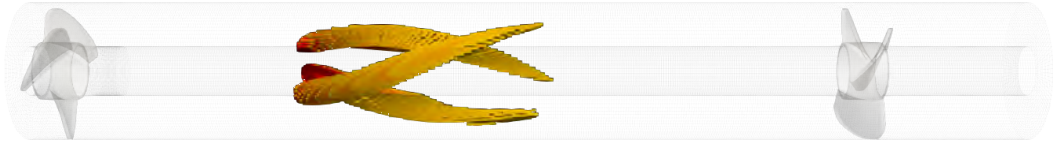

(**f**) (H) - 0.6

Figure 11. Spatial distribution of m_0 for the six simulations. Only volumes with $m_0 > 10^{18}$ particle no./m^3 are shown.

5. Discussion

The CFD-PBM framework developed in this study provides mechanistic insights into $Mg(OH)_2$ precipitation under varying feed concentrations and nozzle configurations. These findings are particularly relevant for the design and optimization of semi-continuous and continuous crystallization/precipitation processes in industrial applications such as wastewater treatment and magnesium recovery. From an industrial perspective, the results highlight the strong dependence of particle formation on mixing intensity and feed positioning. This suggests that engineering modifications, such as optimizing nozzle orientation, implementing multi-inlet configurations, or using recirculation loops, can effectively tailor the local supersaturation profile to favor desirable nucleation, growth, and aggregation pathways. For example, the use of angled or tangential feeds could help in homogenizing mixing zones while mitigating undesired aggregation. However, some limitations must be acknowledged. The current model assumes the PBM is one-way coupled to the flow field, neglecting the potential feedback of high solid loading on hydrodynamics. While this assumption is acceptable for the dilute conditions considered here, it may not hold for larger-scale reactors operating at a much higher throughput and some scale-up factors should be included. Additionally, the computational cost of the CFD-PBM simulations is not excessive, making this framework suitable for further investigations. Each CFD-PBM simulation required approximately 3 to 5 days of wall-

clock time using 16 CPU cores and 64 GB of RAM. This makes the framework tractable for mechanistic investigations and design studies, but potentially too slow for large-scale parameter identification or optimization tasks. Therefore, ongoing work is focused on developing machine learning surrogates to accelerate the design phase, as demonstrated in one of our previous publications [23]. Despite these limitations, the model provides a valuable mechanistic baseline that can be generalized to other precipitation systems, such as $CaCO_3$ and $BaSO_4$.

6. Conclusions

This study presents a CFD-PBM one-way coupled framework tailored toward detailing and optimizing the performance of a novel prototype for the recovery of Mg^{2+} from brines and bitterns. Beyond characterizing the prototype's complex hydrodynamics, we propose a series of modeling strategies and insights that can improve both fundamental understanding and smart reactor design. A key methodological contribution lies in the use of high-fidelity LES simulations to calibrate an RANS model capable of replicating the essential turbulence features at a significantly lower computational cost. This LES-calibrated RANS approach provides a practical yet accurate alternative to screening design variations in complex geometries when experimental validation is lacking. On the process side, our simulations reveal the non-intuitive effects of increased reactant concentrations: while higher molar flow rates nominally boost supersaturation, they can simultaneously hinder mixing, leading to negligible gains in precipitation rate. This highlights the importance of accounting for local micromixing dynamics rather than relying solely on bulk process variables. Furthermore, by varying the orientation and position of the nozzle, we can identify the crucial role of local turbulence dissipation rates in governing nucleation, growth, and aggregation processes. This leads to actionable guidance for reactor optimization: namely, that nozzle placement should be informed by the local turbulent energy dissipation field to maximize precipitation efficiency. This work demonstrates the value of combining advanced CFD modelling with PBM to support the smart manufacturing of crystallization and recovery processes in multiphase, turbulent systems.

7. Patents

The patent can be found through following this link: https://patents.google.com/patent/WO2022238913A1/en (accessed on 2 February 2024) and referring to Bevacqua et al. [26].

Supplementary Materials: The following supporting information can be downloaded at: https://www.mdpi.com/article/10.3390/pr13061721/s1, Figure S1: Monitoring lines selected downstream of the impellers for grid convergence analysis; Figure S2: Mesh visualization along the two monitoring lines for the three grid resolutions.

Author Contributions: Conceptualization, A.R.; methodology, A.R.; software, A.R.; validation, A.R.; formal analysis, A.R. and D.F.; investigation, A.R.; resources, F.V., A.C. and D.M.; data curation, A.R.; writing—original draft preparation, A.R.; writing—review and editing, A.R., F.V., A.C. and D.M.; visualization, A.R. and D.F.; supervision, A.R. and D.M.; project administration, A.C. and D.M.; funding acquisition, A.C. and D.M. All authors have read and agreed to the published version of the manuscript.

Funding: This project has received funding from the European Union's Horizon 2020 research and innovation programme under Grant Agreement No. 869467 (SEArcularMINE). This output reflects only the author's view. The European Health and Digital Executive Agency (HaDEA) and the European Commission cannot be held responsible for any use that may be made of the information contained therein.

Data Availability Statement: Data are available upon request.

Acknowledgments: A heartfelt thank you goes to Ing. Lorena Pasero for the fruitful discussions and feedback on the Design of Simulations. This project has received funding from the European Union's Horizon 2020 research and innovation programme under Grant Agreement No. 869467 (SEArcularMINE). This output reflects only the author's view. The European Health and Digital Executive Agency (HaDEA) and the European Commission cannot be held responsible for any use that may be made of the information contained therein. Computational resources were provided by HPC@POLITO, a project of Academic Computing within the Department of Control and Computer Engineering at the Politecnico di Torino (http://www.hpc.polito.it)).

Conflicts of Interest: Author Fabrizio Vicari was employed by the company ResourSEAs srl. The remaining authors declare that the research was conducted in the absence of any commercial or financial relationships that could be construed as a potential conflict of interest.

Abbreviations

The following abbreviations are used in this manuscript:

CFD	Computational Fluid Dynamics
PBM	Population Balance Model

References

1. Tai, C.M.; Li, R.K. Studies on the impact fracture behaviour of flame retardant polymeric material. *Mater. Des.* **2001**, *22*, 15–19. [CrossRef]
2. Béarat, H.; McKelvy, M.J.; Chizmeshya, A.V.; Sharma, R.; Carpenter, R.W. Magnesium hydroxide dehydroxylation/carbonation reaction processes: Implications for carbon dioxide mineral sequestration. *J. Am. Ceram. Soc.* **2002**, *85*, 742–748. [CrossRef]
3. Chen, X.; Yu, J.; Guo, S. Structure and properties of polypropylene composites filled with magnesium hydroxide. *J. Appl. Polym. Sci.* **2006**, *102*, 4943–4951. [CrossRef]
4. Zhang, S.; Cheng, F.; Tao, Z.; Gao, F.; Chen, J. Removal of nickel ions from wastewater by $Mg(OH)_2$/MgO nanostructures embedded in Al_2O_3 membranes. *J. Alloys Compd.* **2006**, *426*, 281–285. [CrossRef]
5. Gui, H.; Zhang, X.; Dong, W.; Wang, Q.; Gao, J.; Song, Z.; Lai, J.; Liu, Y.; Huang, F.; Qiao, J. Flame retardant synergism of rubber and $Mg(OH)_2$ in EVA composites. *Polymer* **2007**, *48*, 2537–2541. [CrossRef]
6. Kakaraniya, S.; Kari, C.; Verma, R.; Mehra, A. Gas absorption in slurries of fine particles: SO_2-$Mg(OH)_2$-$MgSO_3$ system. *Ind. Eng. Chem. Res.* **2007**, *46*, 1904–1913. [CrossRef]
7. Cao, H.; Zheng, H.; Yin, J.; Lu, Y.; Wu, S.; Wu, X.; Li, B. $Mg(OH)_2$ complex nanostructures with superhydrophobicity and flame retardant effects. *J. Phys. Chem. C* **2010**, *114*, 17362–17368. [CrossRef]
8. Sierra-Fernandez, A.; Gomez-Villalba, L.S.; Milosevic, O.; Fort, R.; Rabanal, M.E. Synthesis and morpho-structural characterization of nanostructured magnesium hydroxide obtained by a hydrothermal method. *Ceram. Int.* **2014**, *40*, 12285–12292. [CrossRef]
9. Song, X.; Tong, K.; Sun, S.; Sun, Z.; Yu, J. Preparation and crystallization kinetics of micron-sized $Mg(OH)_2$ in a mixed suspension mixed product removal crystallizer. *Front. Chem. Sci. Eng* **2013**, *7*, 130–138. [CrossRef]
10. Mullin, J.W. *Crystallization*; Elsevier: Amsterdam, The Netherlands, 2001.
11. Mersmann, A. *Crystallization Technology Handbook*; Marcel Dekker: New York, NY, USA, 2001; p. 832.
12. Baldyga, J.; Podgorska, W.; Pohorecki, R. Mixing-precipitation model with application to double feed semibatch precipitation. *Chem. Eng. Sci.* **1995**, *50*, 1281–1300. [CrossRef]
13. Marchisio, D.L.; Barresi, A.A.; Fox, R.O. Simulation of Turbulent Precipitation in a Semi-batch Taylor-Couette Reactor Using CFD. *AIChE J.* **2001**, *47*, 664–676. [CrossRef]
14. Marchisio, D.L.; Barresi, A.A.; Garbero, M. Nucleation, growth, and agglomeration in barium sulfate turbulent precipitation. *AIChE J.* **2002**, *48*, 2039–2050. [CrossRef]
15. Orlewski, P.M.; Mazzotti, M. Modeling of Mixing-Precipitation Processes: Agglomeration. *Chem. Eng. Technol.* **2020**, *43*, 1029–1039. [CrossRef] [PubMed]
16. Danckwerts, P. The effect of incomplete mixing on homogeneous reactions. *Chem. Eng. Sci.* **1958**, *8*, 93–102. [CrossRef]
17. Becker, G.W.; Larson, M.A. Mixing Effects in Continuous Crystallization. In *Crystallization from Solutions and Melts*; Palermo, J.A., Larson, M.A., Eds.; Springer: Boston, MA, USA, 1969; pp. 14–23. [CrossRef]
18. Battaglia, G.; Romano, S.; Raponi, A.; Volpe, F.; Bellanca, L.; Ciofalo, M.; Marchisio, D.; Cipollina, A.; Micale, G.; Tamburini, A. Mixing phenomena in circular and rectangular cross-sectional T-mixers: Experimental and numerical assessment. *Chem. Eng. Res. Des.* **2024**, *201*, 228–241. [CrossRef]

19. Schikarski, T.; Trzenschiok, H.; Peukert, W.; Avila, M. Inflow boundary conditions determine T-mixer efficiency. *React. Chem. Eng.* **2019**, *4*, 559–568. [CrossRef]
20. Schikarski, T.; Avila, M.; Trzenschiok, H.; Güldenpfennig, A.; Peukert, W. Quantitative modeling of precipitation processes. *Chem. Eng. J.* **2022**, *444*, 136195. [CrossRef]
21. Shiea, M.; Querio, A.; Buffo, A.; Boccardo, G.; Marchisio, D. CFD-PBE modelling of continuous Ni-Mn-Co hydroxide co-precipitation for Li-ion batteries. *Chem. Eng. Res. Des.* **2022**, *177*, 461–472. [CrossRef]
22. Raponi, A.; Romano, S.; Battaglia, G.; Buffo, A.; Vanni, M.; Cipollina, A.; Marchisio, D. Computational Modeling of Magnesium Hydroxide Precipitation and Kinetics Parameters Identification. *Cryst. Growth Des.* **2023**, *23*, 4748–4759. [CrossRef]
23. Raponi, A.; Marchisio, D. Deep learning for kinetics parameters identification: A novel approach for multi-variate optimization. *Chem. Eng. J.* **2024**, *489*, 151149. [CrossRef]
24. Raponi, A.; Achermann, R.; Romano, S.; Trespi, S.; Mazzotti, M.; Cipollina, A.; Buffo, A.; Vanni, M.; Marchisio, D. Population balance modelling of magnesium hydroxide precipitation: Full validation on different reactor configurations. *Chem. Eng. J.* **2023**, *477*, 146540. [CrossRef]
25. Battaglia, G.; Ventimiglia, L.; Vicari, F.; Tamburini, A.; Cipollina, A.; Micale, G. Characterization of $Mg(OH)_2$ powders produced from real saltworks bitterns at a pilot scale. *Powder Technol.* **2024**, *443*, 119918. [CrossRef]
26. Bevacqua, M.; Vassallo, F.; Cipollina, A.; Micale, G.; Tamburini, A.; Papapetrou, M.; Vicari, F. Reactor and Process for the Precipitation of a Solid Product, (ResourSEAs Srl), IT202100012473A. 2021. Available online: https://patents.google.com/patent/WO2022238913A1/en (accessed on 2 February 2024).
27. Maniscalco, F.; Buffo, A.; Marchisio, D.; Vanni, M. Numerical simulation of bubble columns: LES turbulence model and interphase forces blending approach. *Chem. Eng. Res. Des.* **2021**, *173*, 1–14. [CrossRef]
28. Pope, S. Ten Questions Concerning the Large-Eddy Simulation of Turbulent Flows. *New J. Phys.* **2004**, *6*, 35. [CrossRef]
29. David, R.; Marchal, P.; Klein, J.P.; Villermaux, J. Crystallization and precipitation engineering-III. A discrete formulation of the agglomeration rate of crystals in a crystallization process. *Chem. Eng. Sci.* **1991**, *46*, 205–213. [CrossRef]
30. Marchisio, D.L.; Pikturna, J.T.; Fox, R.O.; Vigil, R.D.; Barresi, A.A. Quadrature Method of Moments for Population-Balance Equations. *AlChE J.* **2003**, *49*, 1266–1276. [CrossRef]
31. Romano, S.; Trespi, S.; Achermann, R.; Battaglia, G.; Raponi, A.; Marchisio, D.; Mazzotti, M.; Micale, G.; Cipollina, A. The Role of Operating Conditions in the Precipitation of Magnesium Hydroxide Hexagonal Platelets Using NaOH Solutions. *Cryst. Growth Des.* **2023**, *23*, 6491–6505. [CrossRef]